Terrestrial planet formation by torque-driven convergent migration of planetary embryos (SI)

M. Brož[1], O. Chrenko[1], D. Nesvorný[2], N. Dauphas[3]

[1]*Institute of Astronomy, Charles University, V Holešovičkách 2, 18000 Prague 8, Czech Republic*

[2]*Department of Space Studies, Southwest Research Institute, 1050 Walnut St., Suite 300, Boulder, CO 80302, USA*

[3]*Origins Laboratory, Department of the Geophysical Sciences and Enrico Fermi Institute, The University of Chicago, 5734 South Ellis Av., Chicago, IL 60637, USA*

A Radiation hydrodynamic model

Our current model includes the following set of integro-differential equations (see also [35]):

$$\frac{\partial\Sigma}{\partial t}+\mathbf{v}\cdot\nabla\Sigma=-\Sigma\nabla\cdot\mathbf{v}-\left(\frac{\partial\Sigma}{\partial t}\right)_{\mathrm{acc}}, \tag{1}$$

$$\frac{\partial\mathbf{v}}{\partial t}+\mathbf{v}\cdot\nabla\mathbf{v}=-\frac{1}{\Sigma}\nabla P+\frac{1}{\Sigma}\nabla\cdot\mathsf{T}-\frac{\int\rho\nabla\phi\,\mathrm{d}z}{\Sigma}+\frac{\Sigma_\mathrm{p}}{\Sigma}\frac{\Omega_\mathrm{K}}{\tau}(\mathbf{u}-\mathbf{v}), \tag{2}$$

$$\begin{aligned}\frac{\partial E}{\partial t}+\mathbf{v}\cdot\nabla E &= -E\nabla\cdot\mathbf{v}-P\nabla\cdot\mathbf{v}+Q_\mathrm{visc}+\frac{2\sigma T_\mathrm{irr}^4}{\tau_\mathrm{eff}}-\frac{2\sigma T^4}{\tau_\mathrm{eff}}+\\ &\quad+2H\nabla\cdot\frac{16\sigma\lambda_\mathrm{lim}}{\rho_0\kappa_\mathrm{R}}T^3\nabla T+\sum_i\frac{GM_i\dot{M}_i}{R_iS_\mathrm{cell}}\delta(\mathbf{r}-\mathbf{r}_i),\end{aligned} \tag{3}$$

$$P=\Sigma\frac{RT}{\mu}=(\gamma-1)E, \tag{4}$$

$$\frac{\partial\Sigma_\mathrm{p}}{\partial t}+\mathbf{u}\cdot\nabla\Sigma_\mathrm{p}=-\Sigma_\mathrm{p}\nabla\cdot\mathbf{u}-\left(\frac{\partial\Sigma_\mathrm{p}}{\partial t}\right)_{\mathrm{acc}}-\left(\frac{\partial\Sigma_\mathrm{p}}{\partial t}\right)_{\mathrm{evap}}, \tag{5}$$

$$\frac{\partial\mathbf{u}}{\partial t}+\mathbf{u}\cdot\nabla\mathbf{u}=-\frac{\int\rho_\mathrm{p}\nabla\phi\,\mathrm{d}z}{\Sigma_\mathrm{p}}-\frac{\Omega_\mathrm{K}}{\tau}(\mathbf{u}-\mathbf{v}), \tag{6}$$

$$\dot{M}_i = \iint \left[\left(\frac{\partial \Sigma}{\partial t} \right)_{\rm acc} + \left(\frac{\partial \Sigma_{\rm p}}{\partial t} \right)_{\rm acc} \right] r {\rm d}\theta {\rm d}r \quad \text{for } \forall i \,, \tag{7}$$

$$\begin{aligned} \ddot{\mathbf{r}}_i \;\; = \;\; & -\frac{GM_\star}{r_i^3}\mathbf{r}_i - \sum_{j \neq i} \frac{GM_j}{|\mathbf{r}_i - \mathbf{r}_j|^3}(\mathbf{r}_i - \mathbf{r}_j) + \iiint \frac{\rho \nabla \phi_i \, {\rm d}z}{M_i} r {\rm d}\theta {\rm d}r \; + \\ & + f_z \hat{z} - \frac{1}{2} C \frac{\pi R_i^2}{M_i} \rho |\dot{\mathbf{r}}_i - \mathbf{v}_{\rm cell}| (\dot{\mathbf{r}}_i - \mathbf{v}_{\rm cell}) + \iint \left[\mathbf{v} \left(\frac{\partial \Sigma}{\partial t} \right)_{\rm acc} + \mathbf{u} \left(\frac{\partial \Sigma_{\rm p}}{\partial t} \right)_{\rm acc} \right] r {\rm d}\theta {\rm d}r \\ & \text{for } \forall i \,, \end{aligned} \tag{8}$$

where Σ is the gas surface density, $\mathbf{v}$ gas velocity, $(\partial\Sigma/\partial t)_{\rm acc}$ gas accretion term[36], P vertically integrated pressure, T viscous stress tensor, $\rho = \Sigma/(\sqrt{2\pi}H)\exp[-z^2/(2H^2)]$ gas volumetric density, H scale height, $\phi = \phi_\star + \sum \phi_i$ gravitational potential of the Sun and protoplanets, with a cubic smoothing due to a finite cell size[37] (not H), z vertical coordinate, $\Sigma_{\rm p}$ pebble surface density, $\mathbf{u}$ pebble velocity, $(\partial\Sigma_{\rm p}/\partial t)_{\rm acc}$ pebble accretion term for the Bondi and Hill regimes[38], $\Omega_{\rm K}$ the Keplerian angular velocity, τ the Stokes number of pebbles, E gas internal energy, $Q_{\rm visc}$ viscous heating term[39], σ the Stefan–Boltzmann constant, $T_{\rm irr}$ irradiation temperature[40], $\tau_{\rm eff}$ effective optical depth[41], T gas temperature, $\lambda_{\rm lim}$ flux limiter[42], ρ_0 midplane density, $\kappa_{\rm R}$ the Rosseland opacity, G gravitational constant, M_i protoplanet mass, R_i protoplanet radius, $S_{\rm cell}$ cell area in which it is located, R gas constant, μ mean molecular weight, γ adiabatic index, $\ddot{\mathbf{r}}_i$ acceleration of the body i, with the smoothing applied for the 3rd term; f_z vertical damping[43] (while the horizontal damping is computed self-consistently), C drag coefficient, and $\mathbf{v}_{\rm cell}$ cell velocity.

As the numerical code is based on Fargo[44], it also uses the Fargo algorithm to overcome the time step limitation due to the Keplerian motion at the inner edge of the disk. For the numerical integration of planetary orbits we use the IAS15 integrator from the Rebound package[45], with an adaptive time step to precisely handle close encounters.

The pebble evaporation term is assumed simply as:

$$\left(\frac{\partial \Sigma_{\mathrm{p}}}{\partial t}\right)_{\mathrm{evap}} = f_{\mathrm{ev}} \Sigma_{\mathrm{p}} \mathcal{H}(T - T_{\mathrm{ev}}) \,, \tag{9}$$

where T_{ev} denotes the evaporation temperature, f_{ev} the respective rate, and $\mathcal{H}$ the Heaviside step function. We use this approximation only for a single evaporation line and pebble surface area, instead of chemical equilibrium and Hertz–Knudsen equations. The remaining terms were described in more detail in [35] or [46].

B Limitations of the model

Every model has its own limitations. The Planck opacity κ_{P}, which is hidden in τ_{eff}, is assumed to be the same as the Rosseland opacity κ_{R} for simplicity. These opacities may differ substantially for temperatures $T \simeq 1000\,\mathrm{K}$[47], in particular in stratified 3D disks with hot atmospheres, but it is not our case, except possibly at the inner edge of the disk.

We assume the drag is always in the Epstein regime; the Stokes regime would be necessary for pebble sizes larger than the mean-free path. The condition $2/9 D_{\mathrm{p}} > \ell$ can be fulfilled only in the innermost part of the most massive disk, where $\ell = \mu m_{\mathrm{H}}/(\sigma\rho) \simeq 0.4\,\mathrm{cm}$. Otherwise, it should not affect our simulations. We also use no reduction factor of the accretion rate[48,49], which would be needed for $\tau \gg 1$.

In a complex model ($9 + 4N$ scalar integro-differential equations in our case; N denotes the number of protoplanets) it may be sometimes difficult to recognise which terms induce the behaviour of interest, because all terms are interrelated (by means of Eqs. (1) to (8)). For example,

a question might be, whether the increase of planetary eccentricities e is driven by hydrodynamic phenomena or secular perturbations (or both). For this purpose we are sometimes forced to use simplified models with selected terms switched off, or a limited number of protoplanets ($N = 1$). An example is shown in Figure 1, which confirms that e is increased due to the hot-trail effect.

Although we do compute the gravity of planets acting on pebbles, the gravity of pebbles acting on planets[50] is not included in most of our simulations, because the pebble flux $\dot{M}_\mathrm{p}$ and the pebble-to-gas ratio $\Sigma_\mathrm{p}/\Sigma \simeq 10^{-3}$ to 10^{-2} are generally low, as well as the Stokes number $\tau \simeq 0.01$. For a $M = 1\,M_\mathrm{E}$ planet on a circular fixed orbit, without pebble accretion and without back-reaction on gas, the ratio of torques would be $\Gamma_\mathrm{p}/\Gamma_\mathrm{g} \simeq 0.01$ to 0.1 according to [50], which can be considered negligible. Because the situation is actually more complicated — protoplanets in our simulations are generally eccentric, not fixed, Σ_p is decreased by accretion, and the gas flow $\mathbf{v}$ is changed by the pebble flow $\mathbf{u}$ — we checked that the migration rates do *not* change substantially when the respective term $\iiint \frac{\rho_\mathrm{p} \nabla \phi_i}{M_i} \mathrm{d}z\, r \mathrm{d}\theta \mathrm{d}r$ is added to Eq. (8); see Figure 2.

We assume that all pebbles have the same chemical composition, and we do not track their composition explicitly. For simplicity, we also use a single evaporation temperature for pebbles, corresponding to that of high-temperature minerals (iron, orthopyroxene, olivine). Nevertheless, the integral opacities κ_R contain dust evaporation implicitly, for several distinct minerals (water ice, graphite, and remaining grains in case of [51]; and even more minerals in case of [52]). We can thus 'guess' the chemical composition of pebbles from to the local value of κ_R. The only problem is that we overestimate the pebble fluxes on protoplanets orbiting interior to the evaporation lines, but this is somewhat suppressed by the fact that M_p is a free parameter and we can optionally use

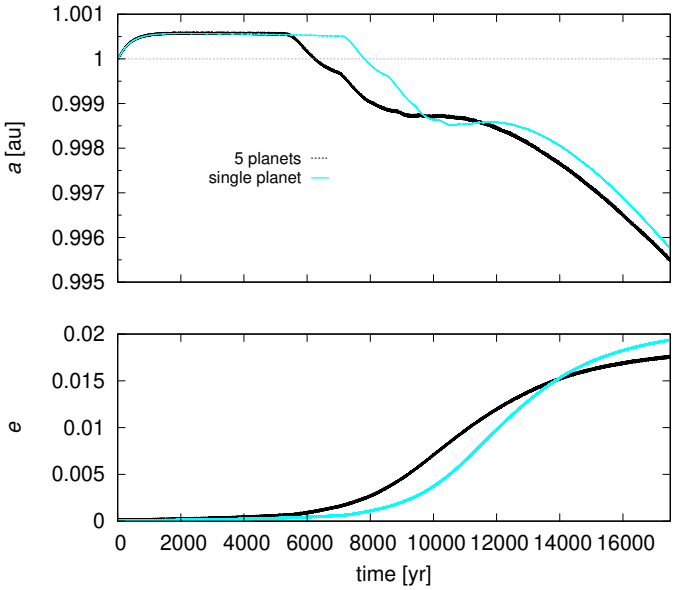

Figure 1: Evolution of semimajor axis a (bottom) and eccentricity e (top) computed for an *isolated* 0.5 Earth-mass body (cyan), in comparison with the same body affected by another 4 protoplanets in the terrestrial region (black). The migration rate is initially the same in both cases, with only minor oscillations in the latter, due to secular perturbations by distant planets. The long-term evolution of eccentricity due to the hot-trail effect is similar, except the single planet exhibits a slower increase of e. The reason is the coupling of secular perturbations (with terms proportional to e) with the hot-trail, which in turn produces a faster increase of e. The evolution of $a(t)$ is then also affected by e.

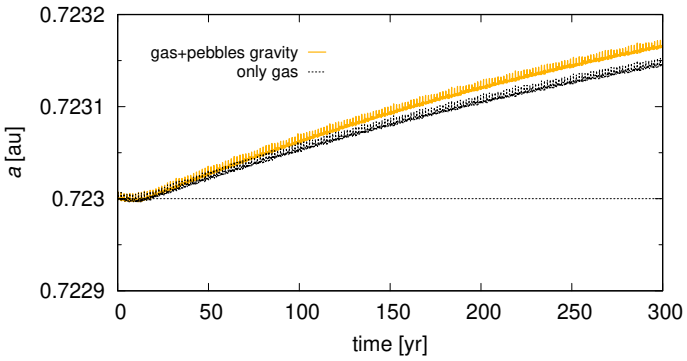

Figure 2: Semimajor axis a vs time t computed for a Venus-mass body affected by the gravity of the gas disk only (dotted) and the gravity of gas plus pebbles (yellow). The difference in the migration rate is at most 10 % which is considered negligible in our context.

a lower value.

C Parameters and initial profiles

The MRI-active disk is defined by its gas flux $\dot{M} = 10^{-8}\,M_\odot\,\mathrm{yr}^{-1}$ and the kinematic viscosity $\nu(r) = 1.1 \times 10^{14}\,\mathrm{cm}^2\,\mathrm{s}^{-1}\,(r/1\,\mathrm{au})^s$, **with the exponent** $s = -2 + 2.5\{1 - \tanh[(1\,\mathrm{au} - r)/(0.15\,\mathrm{au})]\}/2$, in order to obtain **the surface density** Σ similar to a layered-accretion disk[53]. **The profile** $\Sigma(r)$ **is radially increasing across the inner portion of the terrestrial zone,** $r \lesssim 1\,\mathrm{au}$**, and decreasing further out.**

The nominal disk, similar to the MMSN[54], is defined by the **power-law** surface density $\Sigma(r) = \Sigma_0(r/1\,\mathrm{au})^{-1.5}$, with $\Sigma_0 = 750\,\mathrm{g\,cm}^{-2}$, and constant $\nu = 1.5 \times 10^{14}\,\mathrm{cm}^2\,\mathrm{s}^{-1} \doteq 3.3 \times 10^{-5}$ [code units]. This value is compatible with our previous paper[35] focussing on the giant-planet zone, but it is 3 times lower because ν is often parametrized as[55] $\nu = \alpha c_\mathrm{s} H$, where α is yet another

free parameter, c_s the sound speed, and H the vertical scale height. The radial profiles of the last two quantities led us to use lower ν at 1 au. Alternatively, we may use α parameter directly, which would slightly change the profiles. The values corresponding to ν above would be $\alpha \simeq 0.001$ to 0.005.

The common parameters of the simulations are as follows: adiabatic index $\gamma = 1.4$, molecular weight $\mu = 2.4\,\mathrm{g\,mol^{-1}}$, disc albedo $A = 0.5$, vertical opacity drop $c_\kappa = 0.6$, effective temperature of the star $T_\star = 4370\,\mathrm{K}$, stellar radius $R_\star = 1.5\,R_\odot$, softening parameter is $0.5 R_\mathrm{H}$. The entire Hill sphere is considered when calculating disk $\leftrightarrow$ planet interactions. The inner boundary is $r_\mathrm{min} = 0.2\,\mathrm{au}$, outer boundary $r_\mathrm{max} = 2.0\,\mathrm{au}$, a damping boundary condition (e.g. [56]) is used to prevent spurious reflections, and applied up to $1.2 r_\mathrm{min}$ and from $0.9 r_\mathrm{max}$ on; the vertical damping parameter is 0.3, pebble flux $\dot{M}_\mathrm{p} = 2 \times 10^{-4}\,M_\mathrm{E}\,\mathrm{yr}^{-1}$, turbulent stirring parameter $\alpha_\mathrm{p} = 10^{-4}$, which determines the scale height of the pebble disk, $H_\mathrm{p}/H = \sqrt{\alpha_\mathrm{p}/\tau}$, the Schmidt number $\mathrm{Sc} = 1$, pebble coagulation efficiency $\epsilon_\mathrm{p} = 0.5$, pebble bulk density $\rho_\mathrm{p} = 3\,\mathrm{g\,cm^{-3}}$, fragmentation factor $f_\mathrm{f} = 1.0$, fragmentation threshold $10\,\mathrm{m\,s^{-1}}$ [57], turbulence parameter $\alpha_\mathrm{t} = 10^{-3}$, evaporation temperature $T_\mathrm{ev} = 1500\,\mathrm{K}$ [58], evaporation rate $f_\mathrm{ev} = 10^{-3}$, embryo density $\rho_\mathrm{em} = 3\,\mathrm{g\,cm^{-3}}$ (constant).

The spatial discretisation we nominally use is 1024×1536 cells, either with arithmetic spacing, or logarithmic if we need to improve the radial resolution for low-mass embryos. See Appendix E for a convergence test. The discretisation in time is controlled by the CFL condition; the maximal time step is $\Delta t = 0.314159\,[\mathrm{c.u.}] = 1/20\,P_\mathrm{orb}$ at 1.0 au. Orbital elements are output every $20\,\Delta t$, and hydrodynamical fields every $500\,\Delta t$. The nominal time span is approximately

8 kyr. The relative precision of the IAS15 integrator[45] is set to 10^{-9}.

Initial profiles of the gas disk are shown in Figure 3. The respective profiles of the pebble disk are shown in Figure 4. In the terrestrial region their sizes are usually limited by fragmentation[57] and they reach a few centimetres. The Stokes numbers are in the range $\tau \simeq 0.01$ to 0.1, corresponding to a partial coupling between gas and pebbles.

D Supplementary figures

As a supplement to Fig. 2 from the main text, we show migration rates in the MMSN disk in Figure 5. The migration rates of low-mass protoplanets are all negative and the convergence zone does not formally exist. However, these rates do depend on protoplanet mass and they are sufficiently different, $\mathrm{d}a/\mathrm{d}t \doteq -10^{-7}$ to $-10^{-6}\,\mathrm{au\,yr^{-1}}$, such that lunar- and Mars-sized protoplanets approach each other and also concentrate in a narrow annulus. However, the convergence may not be so pronounced if protoplanets do not follow a simple radial dependence of the isolation mass[59].

Alternatively, for wind-driven disks[60] the viscosity in the midplane can be very low, which would also break the convergence zone because the corotation torque is not kept unsaturated. However, we can assume the viscous stress is provided by non-ideal MHD effects[61].

As a supplement to Fig. 3, we show the distribution of the number of planets in our set of N-body simulations, as well as the projectile-to-target mass ratios of Moon-forming impacts in Figure 6.

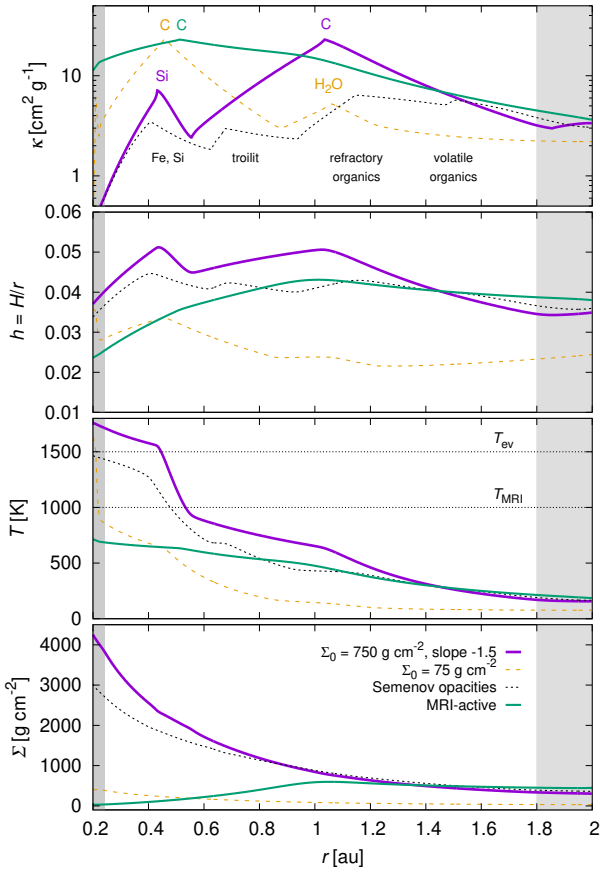

Figure 3: Initial radial profiles of the gas disk, namely the surface density Σ (bottom), temperature T, aspect ratio $h = H/r$, and Rosseland opacity κ (top). They are shown for 4 variants: the nominal disk with $\Sigma_0 = 750\,\mathrm{g\,cm^{-2}}$, the dissipating disk ($\Sigma_0 = 75\,\mathrm{g\,cm^{-2}}$), the nominal one with different opacities[47,52], and the MRI-active disk with the prescribed kinematic viscosity $\nu(r)$. The temperature T_{MRI} indicates a possible value for the onset of magneto-rotational instability, and T_{ev} for the evaporation of (all) pebbles.

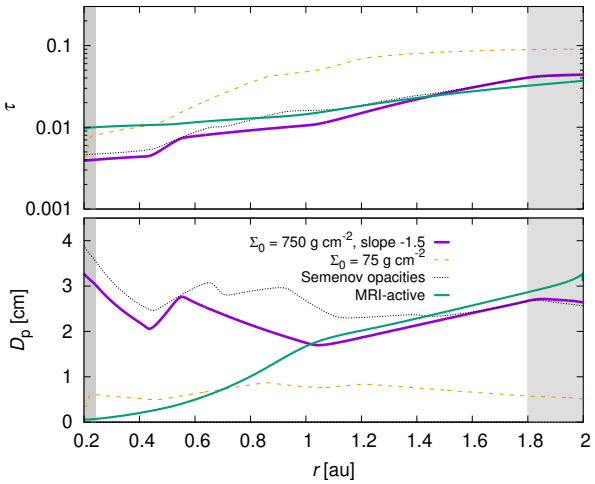

Figure 4: Initial radial profiles of the pebble disk. The pebble size D_p (bottom) and the Stokes number τ (top) are shown for 4 variants: the nominal disk with $\Sigma_0 = 750\,\mathrm{g\,cm^{-2}}$, the dissipating disk ($\Sigma_0 = 75\,\mathrm{g\,cm^{-2}}$), the nominal one with different opacities[47,52], and the MRI-active disk.

In Figure 7, we show both gas and pebble surface densities in the cold dissipating disk ($\Sigma_0 = 75\,\mathrm{g\,cm^{-2}}$), at the end of the respective simulation. Finally, we show the corresponding short-term orbital evolution demonstrating the hot-trail effect, as computed by our hydrodynamical model (Figure 8).

E A convergence test for a Mercury-size body

For the smallest protoplanets of Mercury-size, the resolution of hydrodynamical simulations is critical to correctly capture not only the Lindblad torque (spiral arms) but also the corotation torque, which arises in a relatively narrow range of radii. Alternatively, if we deliberately use a low resolution for some simulation (or a part of it), we have to control and track the respective discretisation error. Our convergence test is thus designed as follows: we assume the same disk as in the main

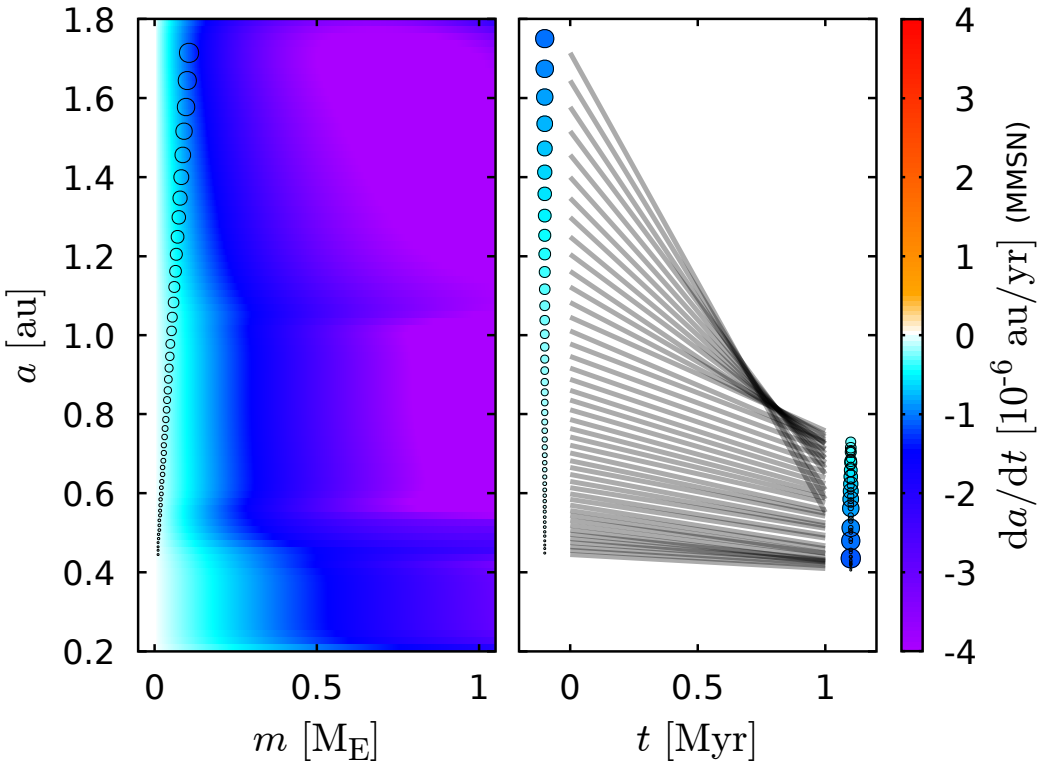

Figure 5: Migration rates $\mathrm{d}a/\mathrm{d}t$ in a gas disk with the surface density $\Sigma = 750\,\mathrm{g\,cm^{-2}}\,r^{-1.5}$, i.e. close to the minimum-mass solar nebula (MMSN[54]). The dependence on the semimajor axis a and protoplanet mass m ([62]; left) and an extrapolated evolution $a(t)$ for lunar- to Mars-size protoplanets (0.01 to $0.1\,M_\mathrm{E}$; right) are shown.

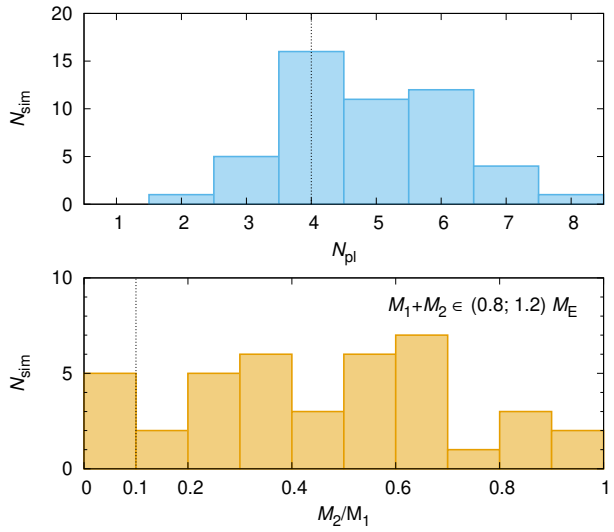

Figure 6: Distribution of the number of planets $N_{\rm pl}$ (top) and projectile-to-target mass ratios M_2/M_1 for Moon-forming impacts (with $M_1 + M_2 \in (0.8; 1.2)\, M_{\rm E}$) (bottom), in our set of N-body simulations with convergent migration.

text, spanning from 0.2 to 2.0 au, Mercury-size protoplanet at 0.387 au, three different resolutions: 1024×1536 (low), 2048×3072 (medium), and 3072×4096 (high), all with a logarithmic radial spacing. This corresponds to approximately 3, 6, 10 cells per Hill sphere, respectively. The results are summarized in Figure 9. It turns out that the migration rate of Mercury-size protoplanet is underestimated by a factor of 2 in low-resolution simulations.

Fortunately, our interpretation of results does not depend sensitively on the particular value of the migration rate of Mercury. It is rather based on the fact that its migration rate (in absolute sense) is significantly smaller that the rate for more massive protoplanets (Mars-size, or later Venus-size), which is true both in low- and high-resolution simulations.

Apart from this convergence test for single planets, we also performed similar tests with

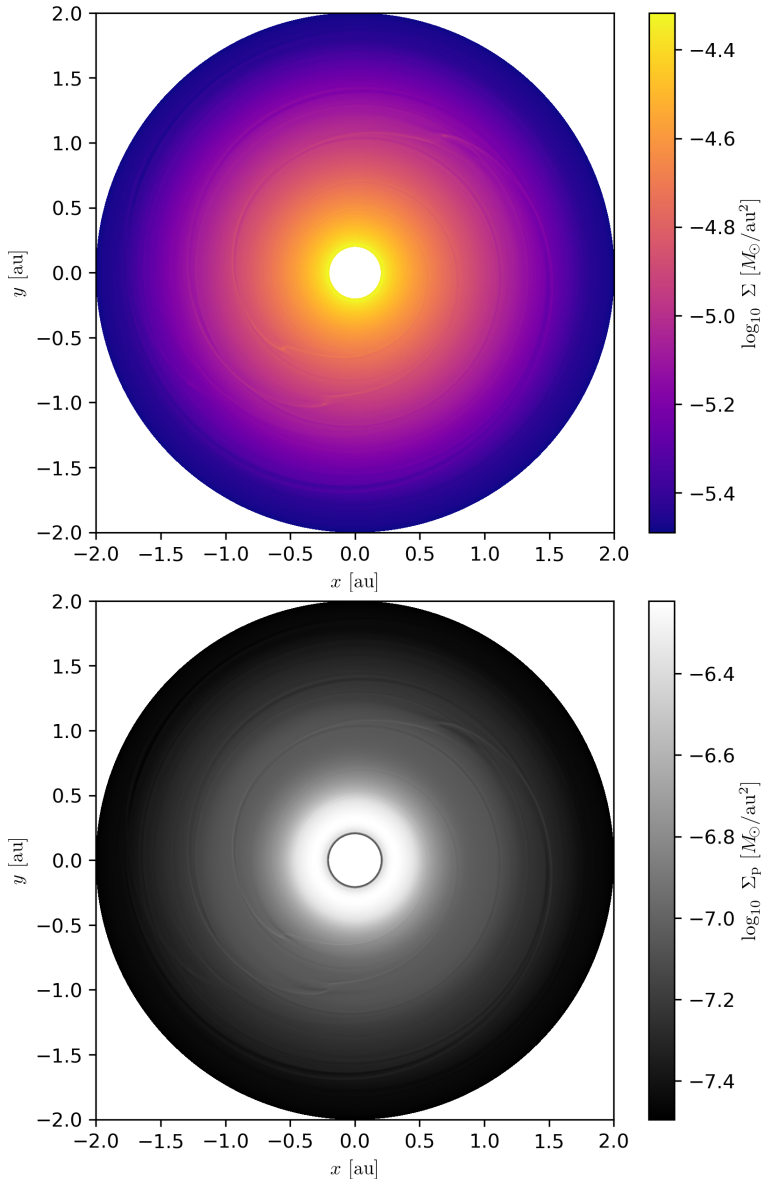

Figure 7: Surface density of gas Σ (left) and pebbles $\Sigma_{\rm p}$ (right) of the dissipating disk with the initial value of $\Sigma_0 = 75\,{\rm g\,cm^{-2}}$. It corresponds to Fig. 4 from the main text (for $t = 0.1\,{\rm kyr}$), but here we show the situation at the end of simulation ($t = 24\,{\rm kyr}$). The structures in both disks can be seen. The hot-trail effect is well developed and the protoplanets gained substantial non-zero eccentricities this way (up to $e \simeq 0.02$). Another contributing factor is the mean-motion resonance 4:3 between protoplanets 4 and 5. The pebble surface density $\Sigma_{\rm p}$ decreases in the vicinity of each planet due to ongoing pebble accretion.

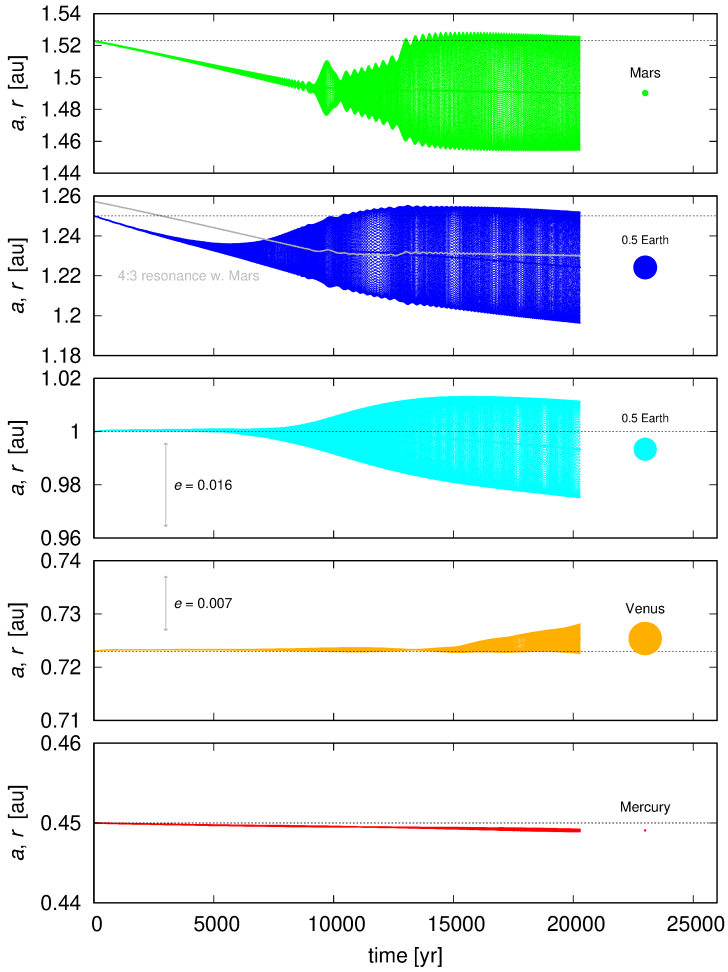

Figure 8: Short-term orbital evolution of 5 terrestrial planets in the cold dissipating disk ($\Sigma_0 = 75\,\mathrm{g\,cm^{-2}}$), as computed by the radiation hydrodynamic (RHD) model. The semimajor axis a and heliocentric distance r vs time t are shown; the oscillations of r correspond to the eccentricity e. The increase of eccentricities by the hot-trail effect up to $e \simeq 0.02$ is comparable to the osculating eccentricities of Venus and Earth, $e = 0.007$ and 0.016 respectively (gray arrows). At $t \doteq 8000\,\mathrm{yr}$ a temporary capture in the 4:3 mean-motion resonance between protoplanets 4 and 5 occurs. Delivery of water by icy pebbles is possible in this situation because the snowline is at approximately 1 au.

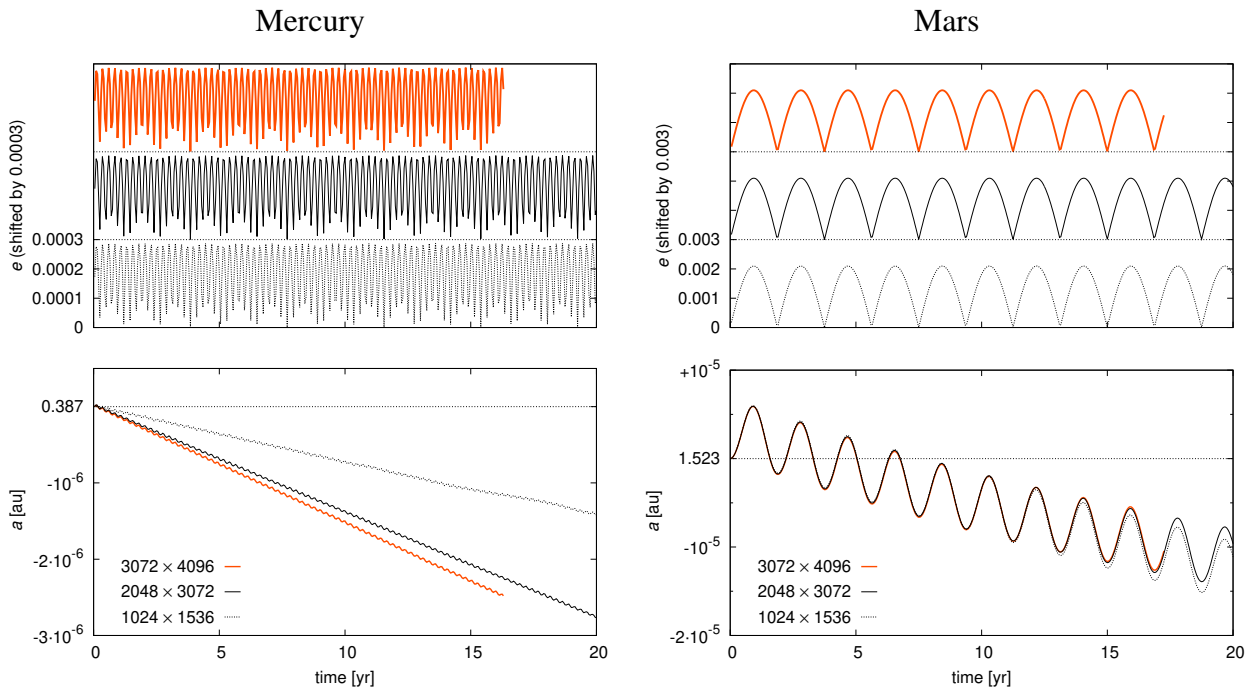

Figure 9: Evolution of semimajor axis a (bottom) and eccentricity e (top) of a Mercury- (left) and Mars-sized bodies (right) for three resolutions: 1024×1536 (low; dashed), 2048×3072 (medium; solid), and 3072×4096 (high; red). In particular, there is a difference in the migration rate of Mercury, which is about 2 times lower for the low-resolution simulation. Nevertheless, it is always significantly smaller than that of Mars (by an order of magnitude). The short-term evolution of eccentricity exhibits the same amplitude for all resolutions.

multiple planets at higher-than-nominal resolution, namely 2048×3072 (medium) instead of 1024×1536 (low), for a relatively short time span only. It turns out the evolution is qualitatively the same, although interacting individual bodies may exhibit different trajectories due to the chaos present in practically all N-body systems.

F Parameters of N-body simulations.

Generally, parameters of the N-body simulations should correspond to the hydrodynamic simulations above, but it is also possible to vary them and perform an extended study (see Sec. G). Here we summarize the nominal values. The disk lifetime is assumed $t_2 - t_1 = 10\,\mathrm{Myr}$; migration time scale is approximated as $\tau(M) = 0.2\,\mathrm{Myr}/(M/M_\mathrm{E})$, migration rate $\dot{a}(a - r_0, \tau) = -\mathrm{sgn}(a - r_0)(a - r_0)^2/\tau$; 0-torque radius $r_0 = 1.1\,\mathrm{au}$ (fixed in this case), however, for the eccentricity $e > 0.02$ we apply a reduction of the torque ($r_0 = 0\,\mathrm{au}$, $\tau = 2\,\mathrm{Myr}/(M/M_\mathrm{E})$), and for $e > 0.06$ the Lindblad torque reversal ($\dot{a} \simeq 0$); damping of eccentricity $\tau_\mathrm{e} = 1\,\mathrm{My}$, which is only active for $e > e_\mathrm{hot} = 0.02$; damping of inclination τ_i is the same, with $i_\mathrm{hot} = 0$. The time step is $\Delta t = 0.01\,\mathrm{yr} \doteq 1/20 P_\mathrm{orb}$ at $0.387\,\mathrm{au}$, with subdivisions during encounters.

The initial conditions for protoplanets were set as follows. We assumed Mercury- to Mars-size protoplanets, with the total mass $M_\mathrm{tot} = 2\,M_\mathrm{E}$, hence the number of protoplanets is 28. Their semimajor axes a were from 0.4 to $1.8\,\mathrm{au}$, so their separations correspond to a constant multiple 9.75 of the mutual Hill radius, $R_\mathrm{HH} = \frac{1}{2}(a + a')(\frac{q+q'}{3})^{1/3}$, the eccentricities $e = 0.01$, the inclinations $i = 0.5°$; all angles (Ω, ω, M) were random. Radii R_i of bodies were computed for the constant bulk density $\rho = 3\,\mathrm{g\,cm^{-3}}$.

The actual transversal, radial and vertical acceleration terms are computed as follows:

$$\ddot{\mathbf{r}}_i = \frac{1}{2}\dot{a}_i \frac{G(M_\oplus + M_i)}{a_i^2 |\mathbf{v}_i|}\,\mathbf{v}_i - 2\mathcal{H}(e_i - e_{\rm hot})\frac{1}{\tau_{\rm e}}\frac{\mathbf{r}_i \cdot \mathbf{v}_i}{r_i^2}\,\mathbf{r}_i - 2\mathcal{H}(i_i - i_{\rm hot})\frac{1}{\tau_{\rm i}}\mathbf{v}_i \cdot \hat{z}\hat{z}\,, \qquad (10)$$

where a_i denotes the semimajor axis of the body i, $\mathbf{r}_i$ its position, $\mathbf{v}_i$ velocity, and $\mathcal{H}$ the Heaviside step function. Optionally, we apply an additional forcing of eccentricity and inclination, simply using $2\mathcal{H} - 1$ instead of $\mathcal{H}$. **Collisions were detected by monitoring positions and perihelia for pairs of bodies. We assumed perfect merging.** In order to account for pebble accretion we increase the mass of bodies as $\dot{M}_i = f\dot{M}_{\rm p}$, where f denotes the filtering factor, reaching up to 5 % and linearly depending on M_i. Because f values are low, we assume the pebble flux $\dot{M}_{\rm p}$ is practically independent of r. **For simplicity, we also assumed that $\dot{M}_{\rm p}$ is independent of t; we tested values in the range 2×10^{-7} to $2\times10^{-5}\,M_{\rm E}\,{\rm yr}^{-1}$. For higher values of $\dot{M}_{\rm p}$, it is necessary to adjust $M_{\rm tot}$.**

G Additional simulations

Unstable disks with variable α-viscosity. The kinematic viscosity ν, or α, is another important parameter which determines the overall structure of the disk, by means of viscous heating. Apart from the (negligible) molecular viscosity, it should account for (unresolved) turbulence and should be thus considered as an eddy viscosity. Its value is not well constrained, also because the underlying turbulence is not fully understood[63–66].

A key question then is whether α is constant, or rather temperature-dependent $\alpha(T)$. If the turbulence in the inner disk is induced by the magneto-rotational instability (MRI) which indeed depends on the ionisation (and T), we should expect a viscosity 'bump'[67]. with a corresponding

drop in the surface density. We already tested a disk with variable α, parametrized as in [67] by $\alpha_{\rm in} = 1.9 \times 10^{-2}$, $\alpha_{\rm out} = 10^{-3}$, $\Delta T = 25\,{\rm K}$, and $T_{\rm MRI} = 1000\,{\rm K}$, and performed a 1D relaxation procedure, but we realised the disk is unstable on the viscous time scale, periodically changing the surface density $\Sigma(r)$ profile and thus protoplanet migration. Such an instability is also present in similar 3D models (Flock, pers. comm.). This may have implications for the terrestrial zone, and it seems worth of a separate study.

N-body simulations vs migration parameters. In order to improve the statistics, we performed N-body simulations of low-mass protoplanets ($< 0.1\,M_{\rm E}$), in which we changed one (or two) parameters. For example, we used Mercury-size protoplanets with $m = 0.05\,M_{\rm E}$; migration time scale $\tau(m) = 0.1\,{\rm My}/(m/M_{\rm E})$, or fixed at 0.1 Myr, 1.0 Myr; migration rate $\dot{a}(a - r_0, \tau)$ linear, or 'sinusoidal'; 0-torque radius as a range 0.7 to $1.0\,{\rm au}$, $r_0(m) = \max(0.7 + 1.5\,(m/M_{\rm E} - 0.8), 0.0)\,{\rm au}$, square-root; damping of eccentricity $\tau_e = 0.1\,{\rm My}$, 0.01, for $e > e_{\rm hot} = 0.04$, or $e(m) = 0.01 + 0.03(m/M_{\rm E} - 0.1)$; similarly damping of inclination τ_i, with $i_{\rm hot} = 0.01$. On the other hand, we used only a single value of the random seed which determines the initial conditions (angles).

As expected, the outcomes of our simulations are more diverse, because the parameters do affect the migration (Figure 10). Nevertheless, even this set often produces Venus and Earth analogues, with Mercury and Mars analogues at the boundaries of the convergence zone. In order to decide which parameters are more suitable for the Solar System, it would be necessary to compute a subset of ~ 50 simulations with multiple random seeds for *every* parameter set, since the evo-

lution is chaotic — especially due to close encounters, which sensitively depend on the geometry — and it is practically impossible that every single simulation ends up as a perfect match. Nevertheless, we find the overall evolution to be systematic and capable of producing terrestrial planets with correct parameters.

Mercury scattering off Venus. The orbit of Mercury with its current osculating eccentricity 0.206 and inclination 7.0° poses a major observational constraint, because it cannot by possibly explained by the hot-trail effect on Mercury which is too weak. One needs a different mechanism and a close encounter with Venus (or a series of them) is a logical choice.

To this point we performed a simplified scattering experiment — we moved Venus as close as $a_\mathrm{V} = 0.44\,\mathrm{au}$; its $e = 0.02$, $I = 0.004\,\mathrm{rad}$ slightly increased due to the hot-trail, acting both in the mid-plane and in the vertical direction[68]. We varied the initial position Mercury in the interval $a_\mathrm{m} \in (0.41; 0.47)\,\mathrm{au}$. We used the Rebound integrator[45] alone, i.e. N-body without any hydrodynamics which is a good approximation for the scattering itself (although cf. [46]; Fig. 6). However, the integration time span was $10\,\mathrm{kyr}$ because the encounters are repeated. Venus is much more massive than Mercury (0.8 vs $0.05\,M_\mathrm{E}$) so its orbit does not change much, but the potential well of Venus is just deep enough to increase Mercury's $e'_\mathrm{m} \simeq 0.14$, $I'_\mathrm{m} \simeq 2^\circ$ (see Figure 11).

While this seems to be slightly lower than the observed osculating values, $e_\mathrm{osc} = 0.206$, $I_\mathrm{osc} = 7.0^\circ$, there are long-term secular perturbation induced by the whole planetary system and our values are just at the lower limit of the respective oscillations, $e \simeq 0.14$ to 0.30, $I \simeq 1^\circ$ to 10° (e.g. [69]). More rigorously, the comparison should be performed with respect to the proper

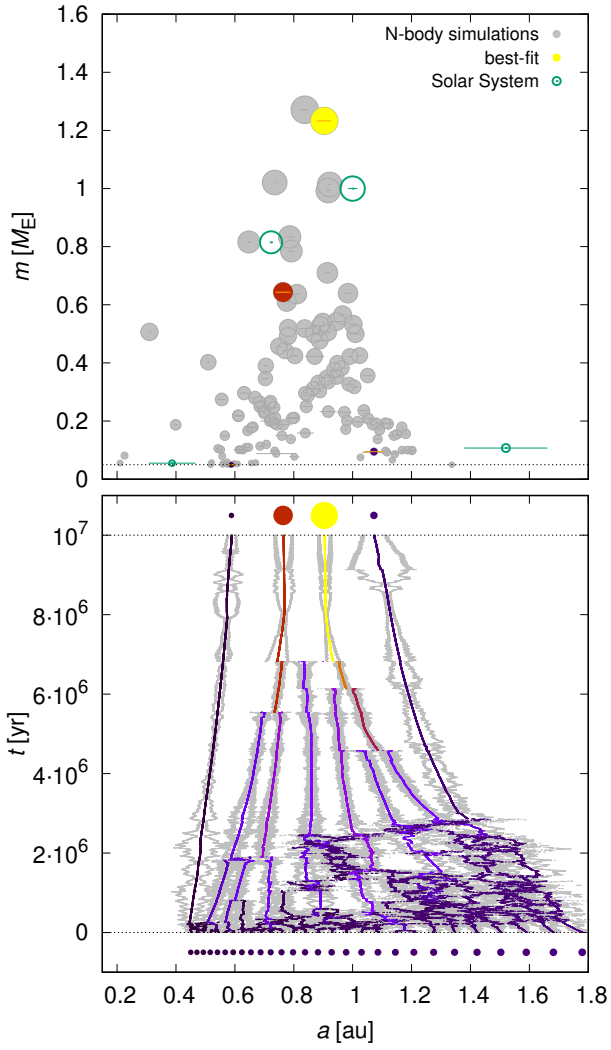

Figure 10: Final mass m vs the final semimajor axis a (top) and a vs time t (bottom), for an extended set of 20 N-body simulations with prescribed migration, with different values of parameters (gray) and one selected 'best-fit' simulation (colour). The Solar System is shown for comparison (green).

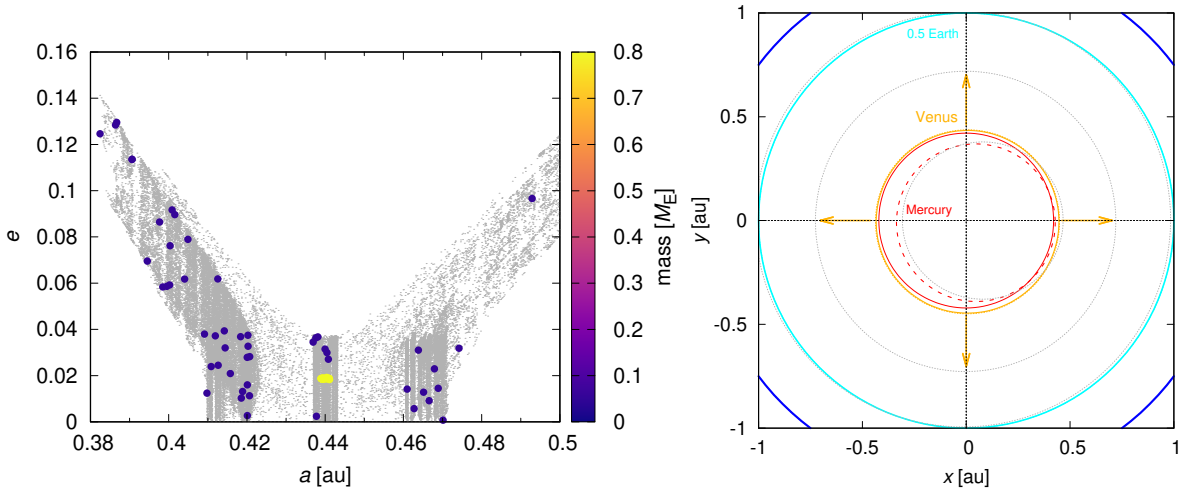

Figure 11: Left: An overview of Mercury orbits (a, e) which resulted from a series of close encounters with Venus (shifted deliberately to $a_{\rm V} = 0.44\,{\rm au}$ and assumed to migrate outwards afterwards). The initial position of Mercury was varied in the interval $a_{\rm m} \in (0.41; 0.47)\,{\rm au}$. The evolution over 10 kyr was computed with a pure N-body model, without any hydrodynamics. The final semimajor axis, eccentricity and inclination of Mercury may reach $a'_{\rm m} = 0.387\,{\rm au}$, $e' \simeq 0.14$, $I' \simeq 2^\circ$. A majority of bodies were scattered, only a minority ended up as coorbitals or merged with Venus, which is indicated by the colour scale (or mass). Right: One example of Mercury scattering off Venus shown in the (x, y) plane. The orbits prior to the scattering (or rather a series of close encounters) are plotted as solid lines; after the scattering as dashed lines. The eccentricity of synthetic Mercury reaches $e' \simeq 0.14$. For comparison, the proper eccentricity of observed Mercury is $e_{\rm prop} = 0.167$. A further increase can be expected due to secular perturbations and corresponding forced oscillations; the osculating $e_{\rm osc} = 0.206$. The current orbits of planets are plotted in gray for comparison. The arrows indicate a subsequent migration of Venus driven by the gas disk torques to its current position ($a = 0.723\,{\rm au}$).

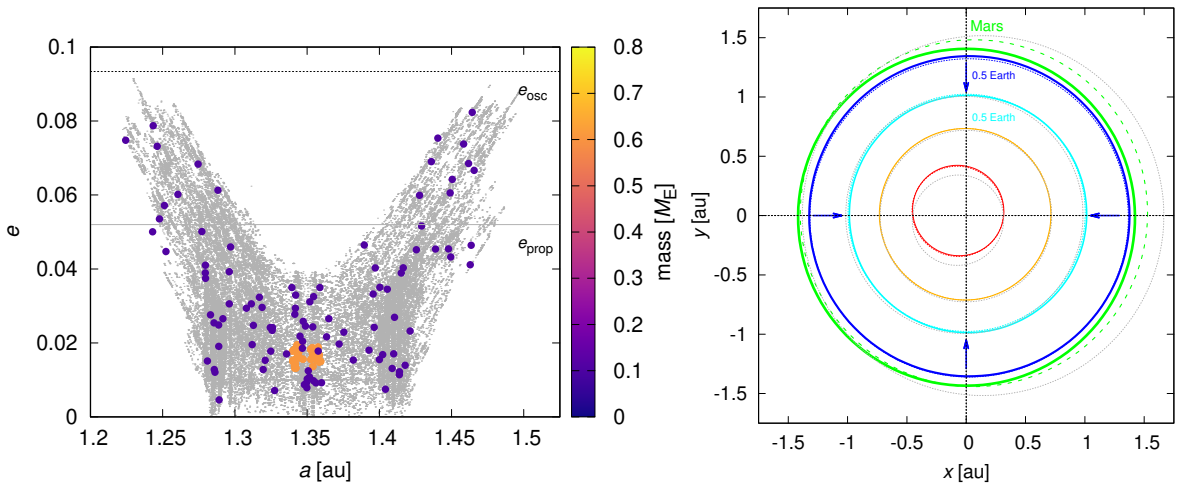

Figure 12: The same as Fig. 11 but for Mars scattering by 0.5 Earth (shifted to $a_{\rm E} = 1.35\,{\rm au}$). The proper eccentricity $e_{\rm prop} = 0.052$ and the osculating $e_{\rm osc} = 0.093$ of observed Mars are indicated by horizontal lines.

elements, $e_{\rm prop} = 0.167$, $I_{\rm prop} = 6.8°$, but the latter depends on the position of the invariable plane.

Finally, Venus and Mercury have to be *detached* from each other otherwise they would still interact. Luckily, the migration of Venus is fast enough, $\mathrm{d}a/\mathrm{d}t \simeq 10^{-6}\,{\rm au\,yr^{-1}}$, and in the correct direction (outward) in the MRI-active disk (Fig. 2 from the main text). It would take only about $(0.723-0.440)/(\mathrm{d}a/\mathrm{d}t) \doteq 10^5\,{\rm yr}$ to migrate to its current position, $a_{\rm V} = 0.723\,{\rm au}$. Consequently, the scattering by Venus is a very natural explanation for the origin of Mercury's orbit. Alternatively, see [70].

Similar arguments are also valid for Mars (see Figure 12).

Orbital elements changes by impacts. To verify changes of the semimajor axis, eccentricity, and inclination due to mutual collisions of protoplanets, we may use the Gauss equations:

$$\Delta a = \frac{2}{n\eta}[\Delta v_{\rm T} + e(\Delta v_{\rm T}\cos f + \Delta v_{\rm R}\sin f)]\,, \tag{11}$$

$$\Delta e = \frac{\eta}{na}[\Delta v_{\rm R}\sin f + \Delta v_{\rm T}(\cos f + \cos E)]\,, \tag{12}$$

$$\Delta i = \frac{1}{na\eta}\Delta v_{\rm W}\frac{r}{a}\cos(\omega + f)\,, \tag{13}$$

where $\Delta v_{\rm R}$, $\Delta v_{\rm T}$, $\Delta v_{\rm W}$ denote the radial, transversal and vertical components of the velocity difference, n mean motion, $\eta \equiv \sqrt{1-e^2}$, f true anomaly, E eccentric anomaly and ω argument of pericentre.

For a canonical Moon-forming impact with masses $m_2 \simeq 0.1\,M_{\rm E}$, $m_1 \simeq 1.0\,M_{\rm E} - m_2$, $a = 1\,{\rm au}$, $e = 0.04$, and geometry $f = 0$, $E = 0$, $\omega = 0$, we may estimate the velocity difference $\Delta v \simeq (m_2/m_1)na(\sqrt{(1+e)/(1-e)} - 1) = 0.13\,{\rm km\,s^{-1}} = 0.01\,v_{\rm esc}$[1] and, assuming the velocity components are of the same order, then $\Delta a \simeq 0.009\,{\rm au}$, $\Delta e \simeq 0.009$, $\Delta i \simeq 0.004\,{\rm rad}$, which can be considered small compared to changes induced by hydrodynamics (Type-I migration, damping, the hot-trail effect). On contrary, for an half-Earth impact[71], much larger changes can be expected, $\Delta a \simeq 0.082\,{\rm au}$, $\Delta e \simeq 0.078$, $\Delta i \simeq 0.039$. However, if they occur early in a gas disk, they do not matter much, because the final values are regulated by hydrodynamics anyway.

Depleted asteroid belt. Apart from the terrestrial convergence zone, there is another one beyond the snowline in the giant-planet zone[35]. The region between them, where the current main asteroid belt is located, can be logically considered a *divergence* zone.[72] To verify this point, we prepared

[1] although the true impact velocity is by $v_{\rm esc}$ larger due to gravitational focussing

another simulation with 20 Mars-size protoplanets, spanning 1.5 to 4 au with spacing of 5 mutual Hill radii, and supplemented by 100 of $D = 100\,\mathrm{km}$ asteroids, as representatives of the former main-belt population. The disk is an extension of the nominal disk with the same Σ_0 as above. We confirm that out of 20 protoplanets most of them migrate away, at a rate $\mathrm{d}a/\mathrm{d}t \doteq 3 \times 10^{-6}\,\mathrm{au\,yr^{-1}}$, and the respective zone is divergent. Moreover, if the runaway growth occurs in both convergence zones, the mass depletion in between can easily reach a factor of 100 (as in [46]; Fig. 20).

Inclined asteroid belt. On their way, protoplanets excite asteroids and virialisation between high- and low-mass bodies, close encounters, and mean-motion resonances push both e and I up to 0.1 and $3°$, respectively, in the course of time (Figure 13). A damping of e and I due to density waves[43] is not efficient for asteroids (having a small factor $m/M_\odot$). On the other hand, aerodynamic drag is not yet strong enough, having a time scale of $\tau_\mathrm{drag} \simeq 1\,\mathrm{Myr}$ for $D = 100\,\mathrm{km}$ bodies. The time span of our simulation ($24\,\mathrm{kyr}$) is again relatively short, but if we extrapolate to $1\,\mathrm{au}/(\mathrm{d}a/\mathrm{d}t) \doteq 3 \times 10^5\,\mathrm{yr}$, assuming a square-root dependence $\sqrt{t}$ suitable for a random-walk process, it would lead to the final $e \simeq 0.3$ and $I \simeq 10°$, in agreement with observations. A single embryo remaining close to the (unstable) 0-torque radius, may be eliminated later, when the disk structure changes (e.g. due to decreasing Σ), or eventually by giant-planet migration which is needed to shape the Kuiper belt[73].

H Geochemical constraints

There are several lines of evidence that protoplanets formed early. For example, ^{182}Hf-^{182}W systematics applied to SNC meteorites indicates Mars formed on a time scale of only 2 My[74]. Ratios

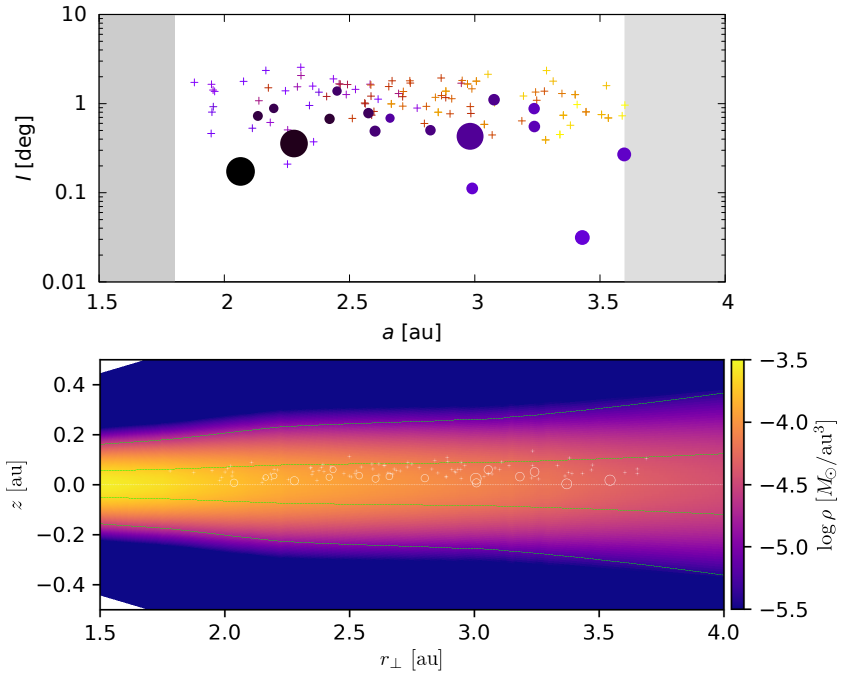

Figure 13: Asteroid belt region in which Mars-sized protoplanets and $D = 100\,\mathrm{km}$ asteroids mutually interact, shown in the semimajor axis a vs inclination I (top) and the gas volumetric density $\rho(r_\perp, z)$ plots (bottom), given by the exponential profile and the local scale height H. Initial conditions were with low $I < 0.01°$, the situation corresponds to $t = 24\,\mathrm{kyr}$. We assume the nominal disk with $\Sigma_0 = 750\,\mathrm{g\,cm^{-2}}$, only extended up to 4 au. According to our hydrodynamical model, the protoplanets migrate at a rate of the order of $3 \times 10^{-6}\,\mathrm{au\,yr^{-1}}$, and they slowly move away; the asteroid belt is thus effectively a *divergence* zone. On the way, they scatter the asteroids, and push them to higher $I \simeq 3°$ (and also $e \simeq 0.1$). If we extrapolate this random-walk evolution up to $t = 300\,\mathrm{kyr}$, assuming $\sqrt{t}$ dependence, it may reach the observed values $I \simeq 10°$ (and $e \simeq 0.3$).

of ^{3}He/^{22}Ne and ^{20}Ne/^{22}Ne in Earth's mantle can be explained by the dissolution of nebular gas in magma oceans on Earth or precursor protoplanets.[75,76]. Similarly, the atmospheric ratios of ^{20}Ne/^{22}Ne and ^{36}Ar/^{38}Ar of Venus indicate escape of a 100-bar primordial (H_2) atmosphere, which can only be captured from the nebula if protoplanets were massive, i.e. $> 0.6\,M_{\rm E}$[77].

Our simulation predict the rapid growth of planets, which can be punctuated by a late giant impact long after dissipation of nebular gas. We used the geochemical model for the Hf/W system[78,79] to evaluate whether our N-body accretional simulations are consistent with the observed anomaly of radiogenic tungsten ^{182}W, $\varepsilon_{182\rm W} \equiv \left\{ \frac{[^{182}{\rm W}/^{184}{\rm W}]}{[^{182}{\rm W}/^{184}{\rm W}]_{\rm CHUR}} - 1 \right\} \cdot 10^4 = 1.9 \pm 0.1$ [80], where CHUR denotes the chondritic uniform reservoir. We used the accretion histories of Earth analogs obtained in our *SyMBA* simulations, and assumed either a constant silicate/metal partitioning coefficient, $D_{\rm W} = 31$, or a variable $D_{\rm W}$, which depends on the mass m of the growing Earth according to the formula:

$$D_{\rm W}(m) = \min(\exp(19.26\,m + 9.03), \exp(3.85\,m^2 - 11.52\,m + 10.49))\,, \qquad (14)$$

obtained from data sent to us by R. Fischer[81] that correspond to the 3 simulations depicted in their Fig. 1 (see Figure 14).

Our results for 4- and 5-planet systems are shown in Figure 15. The cases with 4 planets and no late impacts ($\sim 30\,\%$ of the simulations) exhibit much higher final anomalies (12–14) than measured. For the cases with 5 planets (another $\sim 30\,\%$), we continued our N-body simulations **without migration, but with Jupiter and Saturn on fixed (current) orbits, for additional 300 Myr to test the stability of the terrestrial system (see Figure 16). Systems often end up with 4 planets, as needed. Collisions occur randomly over this interval; they are common**

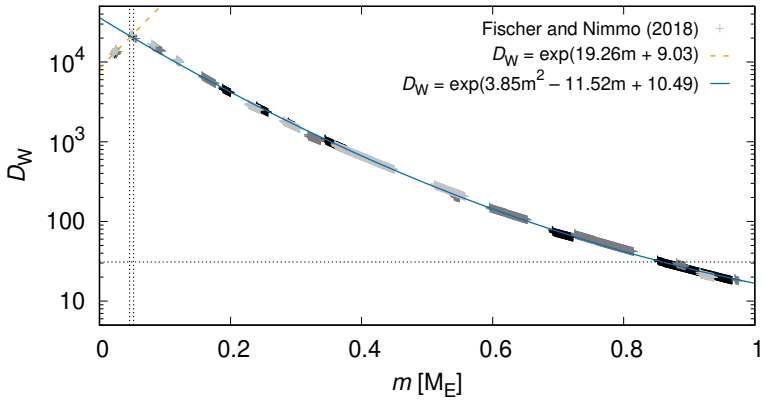

Figure 14: Variable partitioning coefficient of tungsten $D_{\rm W}$ as a function of mass m of the growing Earth. Data (crosses) from ref. [81]; fits (lines) correspond to Eq. (14).

until $\sim 60\,{\rm Myr}$**. Consequently, we** found a very wide range of $\varepsilon_{182{\rm W}}$ values (**similarly** as in [81]; Fig. 5 therein).

In order to have better control of $\varepsilon_{182{\rm W}}$**, we therefore preferred** to prescribe a late Moon-forming impact at $t_{\rm Moon}$. The best results were obtained with $t_{\rm Moon} \simeq 45$ Myr, where practically all results are compatible with observations (Figure 15, right column). This is close to a recent estimate of the time of Moon formation $\simeq 50\,{\rm Myr}$ inferred from Hf-W systematics of lunar rocks ([82]; see however [83,84]). For variable $D_{\rm W}(m)$, there would be even higher anomaly, because initially $D_{\rm W} \gg 31$, the fractionation $f^{\rm Hf/W} \gg 15$, and the derivative is $\dot{\varepsilon}_{182{\rm W}} \propto Q^{\star}_{\rm W} f^{\rm Hf/W}$ ([78]; see Figure 17); this would require the relative mass ratio of impactors 0.33 to half-Earths[71], which are quite common in our simulations with convergent migration (as already demonstrated in Figure 6). Earlier impacts would also require more massive impactors, but there is a lower limit at approximately 30 Myr (for half-Earths) and an upper limit at 60 Myr, provided that the effects of the late veneer were minor. Indeed, the highly siderophile element (HSE) content in Earth's man-

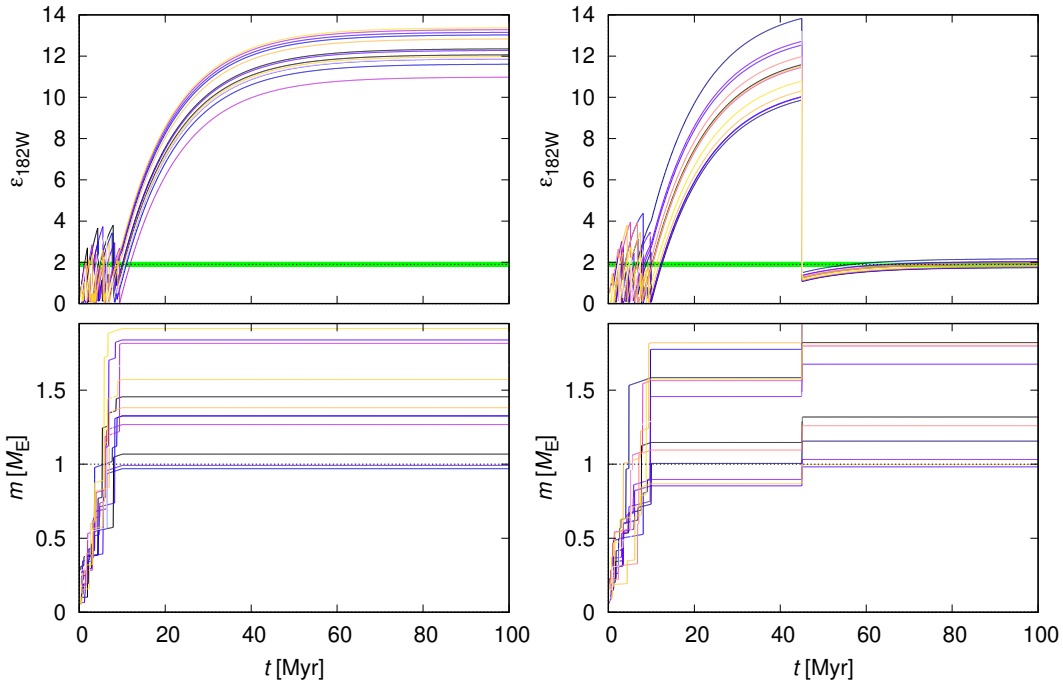

Figure 15: Accretion history $m(t)$ (bottom) and tungsten anomaly $\varepsilon_{182\mathrm{W}}$ (top) for a subset of N-body simulations ending with 4 (left) or 5 planets (right). Colours correspond to individual simulations. The observed value of $\varepsilon_{182\mathrm{W}}$ and its uncertainty is plotted as a green strip. In this test, the partitioning coefficient of tungsten D_{W} was assumed to be constant and the relative impactor size is ~ 0.15.

tle suggests the late veneer mass up to $0.005\,M_{\mathrm{E}}$[85,86] and accounting for this changes $\varepsilon_{182\mathrm{W}}$ by only < 0.1.

I Additional implications

Small Mars. For Mars, there is an additional circumstance, which contributes to its small size (apart from being at the edge of the convergence zone). Normally, pebble accretion proceeds for each planet in parallel and the surface density of pebbles Σ_{p} decreases only by a few per cent,

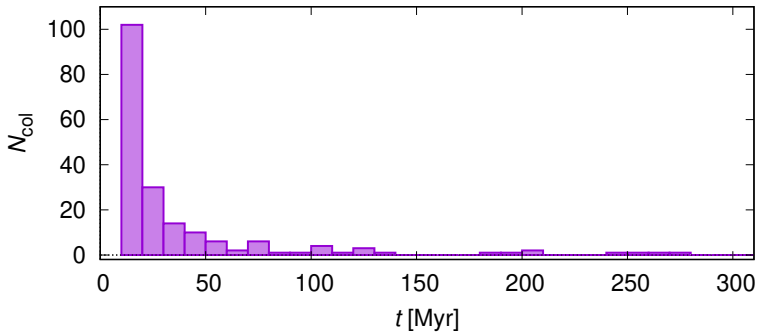

Figure 16: **Distribution of the number of collisions $N_{\rm col}$ in the course of time t for the whole set of 100 N-body simulations, computed without migration and with Jupiter and Saturn, from 10 to 310 Myr. Collisions are common until** $\sim 60\,{\rm Myr}$

according to our estimate of the filtering factors (0.5 to 8 % for Mercury- to Venus-size). But if pebbles are formed *only* within the terrestrial region (as a whole), or when the flux of pebbles $\dot{M}_{\rm p}$ becomes limited (e.g. by the gas giant core), or exhausted in the course of time, the amount of inward-drifting pebbles beyond the orbit is Mars is low, and a logical outcome could be small Mars.

Carbon corrosion. According to Zhu or Semenov opacities[51,52], there is an important transition due to carbon corrosion (or refractory organics). Pebbles remain carbon rich until they reach about 1 au, depending on the disk profile. These pebbles are constantly reprocessed, because the pebble size is fragmentation limited[57], so even carbon incorporated into pebbles can be eliminated on the time scale shorter than drift. Although we do not track the chemical composition explicitly, only implicitly in terms of κ, an outcome could be the carbon-poor composition of Earth[87].

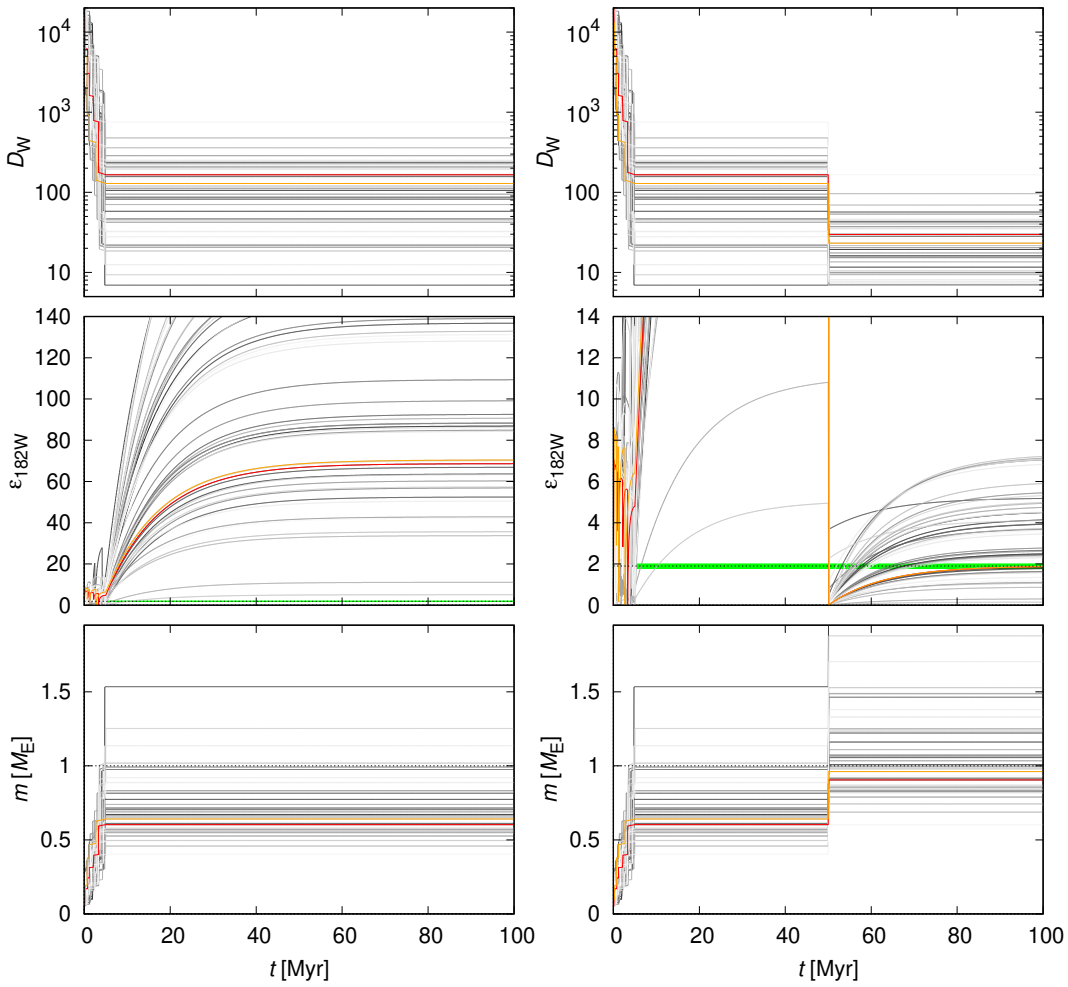

Figure 17: The same as Fig. 15, but with the partitioning coefficient $D_{\rm W}$ as a function of planet mass m[81], and the relative late impactor size ~ 0.33.

Dry Venus. A standard explanation for the non-existence of water vapour on Venus is the runaway greenhouse effect, followed by a dissociation of $\mathrm{H_2O}$, an escape of hydrogen, and a drag-off of oxygen atoms[88], needed to explain the low abundance of oxygen in the atmosphere. Alternatively, if the snowline was always located above 0.7 au, Venus naturally could not accrete icy pebbles and remained dry. The runaway greenhouse effect in its atmosphere then would not involve water vapour.

Dry inner belt. Pebble accretion is also inefficient for $D = 100\,\mathrm{km}$ asteroids and when icy pebbles drift around, a vast majority is not captured. Even Ceres with its mass $1.5 \times 10^{-4}\,M_\mathrm{E}$ is well within the Bondi regime of accretion; the transition to the Hill regime occurs at approximately $10^{-2}\,M_\mathrm{E}$. Moreover, by that time all asteroids are excited to high inclinations $I \gg I_\mathrm{p} \doteq 0.005\,\mathrm{rad} = 0.29^\circ$ and orbit above/below the pebble disk (Fig. 13), which drastically reduces the efficiency of accretion. The inner-main-belt asteroids thus could remain dry too.

35. Chrenko, O., Brož, M. & Lambrechts, M. Eccentricity excitation and merging of planetary embryos heated by pebble accretion. *Astron. Astrophys.* **606**, A114 (2017). 1706.06329.

36. Kley, W. Mass flow and accretion through gaps in accretion discs. *Mon. Not. R. Astron. Soc.* **303**, 696–710 (1999).

37. Klahr, H. & Kley, W. 3D-radiation hydro simulations of disk-planet interactions. I. Numerical algorithm and test cases. *Astron. Astrophys.* **445**, 747–758 (2006).

38. Lambrechts, M. & Johansen, A. Rapid growth of gas-giant cores by pebble accretion. *Astron. Astrophys.* **544**, A32 (2012). 1205.3030.

39. Mihalas, D. & Weibel Mihalas, B. *Foundations of radiation hydrodynamics* (Oxford Univ. Press, 1984).

40. Chiang, E. I. & Goldreich, P. Spectral Energy Distributions of T Tauri Stars with Passive Circumstellar Disks. *Astrophys. J.* **490**, 368–376 (1997).

41. Hubený, I. Vertical structure of accretion disks - A simplified analytical model. *Astrophys. J.* **351**, 632–641 (1990).

42. Kley, W. Radiation hydrodynamics of the boundary layer in accretion disks. I - Numerical methods. *Astron. Astrophys.* **208**, 98–110 (1989).

43. Tanaka, H. & Ward, W. R. Three-dimensional Interaction between a Planet and an Isothermal Gaseous Disk. II. Eccentricity Waves and Bending Waves. *Astrophys. J.* **602**, 388–395 (2004).

44. Masset, F. FARGO: A fast eulerian transport algorithm for differentially rotating disks. *Astron. Astrophys. Suppl. Ser.* **141**, 165–173 (2000). astro-ph/9910390.

45. Rein, H. & Spiegel, D. S. IAS15: a fast, adaptive, high-order integrator for gravitational dynamics, accurate to machine precision over a billion orbits. *Mon. Not. R. Astron. Soc.* **446**, 1424–1437 (2015). 1409.4779.

46. Brož, M., Chrenko, O., Nesvorný, D. & Lambrechts, M. Dynamics of multiple protoplanets embedded in gas and pebble discs and its dependence on Σ and ν parameters. *Astron. Astrophys.* **620**, A157 (2018). 1810.03385.

47. Malygin, M. G., Kuiper, R., Klahr, H., Dullemond, C. P. & Henning, T. Mean gas opacity for circumstellar environments and equilibrium temperature degeneracy. *Astron. Astrophys.* **568**, A91 (2014). 1408.3377.

48. Ormel, C. W. & Klahr, H. H. The effect of gas drag on the growth of protoplanets. Analytical expressions for the accretion of small bodies in laminar disks. *Astron. Astrophys.* **520**, A43 (2010). 1007.0916.

49. Ida, S., Guillot, T. & Morbidelli, A. The radial dependence of pebble accretion rates: A source of diversity in planetary systems. I. Analytical formulation. *Astron. Astrophys.* **591**, A72 (2016). 1604.01291.

50. Benítez-Llambay, P. & Pessah, M. E. Torques Induced by Scattered Pebble-flow in Protoplanetary Disks. *Astrophys. J. Lett.* **855**, L28 (2018). 1801.07913.

51. Zhu, Z., Hartmann, L., Nelson, R. P. & Gammie, C. F. Challenges in Forming Planets by Gravitational Instability: Disk Irradiation and Clump Migration, Accretion, and Tidal Destruction. *Astrophys. J.* **746**, 110 (2012). 1111.6943.

52. Semenov, D., Henning, T., Helling, C., Ilgner, M. & Sedlmayr, E. Rosseland and Planck mean opacities for protoplanetary discs. *Astron. Astrophys.* **410**, 611–621 (2003). astro-ph/0308344.

53. Kretke, K. A. & Lin, D. N. C. The Importance of Disk Structure in Stalling Type I Migration. *Astrophys. J.* **755**, 74 (2012). 1205.4014.

54. Hayashi, C. Structure of the Solar Nebula, Growth and Decay of Magnetic Fields and Effects of Magnetic and Turbulent Viscosities on the Nebula. *Progress of Theoretical Physics Supplement* **70**, 35–53 (1981).

55. Shakura, N. I. & Sunyaev, R. A. Black holes in binary systems. Observational appearance. *Astron. Astrophys.* **24**, 337–355 (1973).

56. Kley, W. & Dirksen, G. Disk eccentricity and embedded planets. *Astron. Astrophys.* **447**, 369–377 (2006).

57. Birnstiel, T., Klahr, H. & Ercolano, B. A simple model for the evolution of the dust population in protoplanetary disks. *Astron. Astrophys.* **539**, A148 (2012). 1201.5781.

58. Pollack, J. B. *et al.* Composition and radiative properties of grains in molecular clouds and accretion disks. *Astrophys. J.* **421**, 615–639 (1994).

59. Walsh, K. J. & Levison, H. F. Planetesimals to terrestrial planets: Collisional evolution amidst a dissipating gas disk. *Icarus* **329**, 88–100 (2019).

60. Ogihara, M., Kokubo, E., Suzuki, T. K. & Morbidelli, A. Formation of the terrestrial planets in the solar system around 1 au via radial concentration of planetesimals. *Astron. Astrophys.* **612**, L5 (2018). 1804.02361.

61. McNally, C. P., Nelson, R. P., Paardekooper, S.-J., Gressel, O. & Lyra, W. Low mass planet migration in Hall-affected disks. In *Journal of Physics Conference Series*, vol. 1031 of *Journal of Physics Conference Series*, 012007 (2018). 1806.06960.

62. Paardekooper, S.-J., Baruteau, C. & Kley, W. A torque formula for non-isothermal Type I planetary migration - II. Effects of diffusion. *Mon. Not. R. Astron. Soc.* **410**, 293–303 (2011). 1007.4964.

63. Nelson, R. P., Gressel, O. & Umurhan, O. M. Linear and non-linear evolution of the vertical shear instability in accretion discs. *Mon. Not. R. Astron. Soc.* **435**, 2610–2632 (2013). 1209.2753.

64. Klahr, H. H. & Bodenheimer, P. Turbulence in Accretion Disks: Vorticity Generation and Angular Momentum Transport via the Global Baroclinic Instability. *Astrophys. J.* **582**, 869–892 (2003). astro-ph/0211629.

65. Balbus, S. A. & Hawley, J. F. A powerful local shear instability in weakly magnetized disks. I - Linear analysis. II - Nonlinear evolution. *Astrophys. J.* **376**, 214–233 (1991).

66. Bae, J., Nelson, R. P. & Hartmann, L. The Spiral Wave Instability Induced by a Giant Planet. I. Particle Stirring in the Inner Regions of Protoplanetary Disks. *Astrophys. J.* **833**, 126 (2016). 1610.08502.

67. Flock, M., Fromang, S., Turner, N. J. & Benisty, M. Radiation Hydrodynamics Models of the Inner Rim in Protoplanetary Disks. *Astrophys. J.* **827**, 144 (2016). 1604.04601.

68. Eklund, H. & Masset, F. S. Evolution of eccentricity and inclination of hot protoplanets embedded in radiative discs. *Mon. Not. R. Astron. Soc.* **469**, 206–217 (2017). 1704.01931.

69. Laskar, J. Secular evolution of the solar system over 10 million years. *Astron. Astrophys.* **198**, 341–362 (1988).

70. Roig, F., Nesvorný, D. & DeSouza, S. R. Jumping Jupiter Can Explain Mercury's Orbit. *Astrophys. J.* **820**, L30 (2016). 1603.02502.

71. Canup, R. M. *et al.* Origin of the Earth and Moon. *New Views of the Moon II* (2019).

72. Bitsch, B., Morbidelli, A., Lega, E. & Crida, A. Stellar irradiated discs and implications on migration of embedded planets. II. Accreting-discs. *Astron. Astrophys.* **564**, A135 (2014). 1401.1334.

73. Nesvorný, D. & Vokrouhlický, D. Neptune's Orbital Migration Was Grainy, Not Smooth. *Astrophys. J.* **825**, 94 (2016). 1602.06988.

74. Dauphas, N. & Pourmand, A. Hf-W-Th evidence for rapid growth of Mars and its status as a planetary embryo. *Nature* **473**, 489–492 (2011).

75. Tucker, J. M. & Mukhopadhyay, S. Evidence for multiple magma ocean outgassing and atmospheric loss episodes from mantle noble gases. *Earth and Planetary Science Letters* **393**, 254–265 (2014). 1403.0806.

76. Wu, J. *et al.* Origin of Earth's Water: Chondritic Inheritance Plus Nebular Ingassing and Storage of Hydrogen in the Core. *Journal of Geophysical Research (Planets)* **123**, 2691–2712 (2018).

77. Lammer, H. *et al.* Origin and evolution of the atmospheres of early Venus, Earth and Mars. *Astron. Astrophys. Rev.* **26**, 2 (2018).

78. Yu, G. & Jacobsen, S. B. Fast accretion of the Earth with a late Moon-forming giant impact. *Proceedings of the National Academy of Science* **108**, 17604–17609 (2011).

79. Jacobsen, S. B. The Hf-W Isotopic System and the Origin of the Earth and Moon. *Annual Review of Earth and Planetary Sciences* **33**, 531–570 (2005).

80. Kleine, T., Münker, C., Mezger, K. & Palme, H. Rapid accretion and early core formation on asteroids and the terrestrial planets from Hf-W chronometry. *Nature* **418**, 952–955 (2002).

81. Fischer, R. A. & Nimmo, F. Effects of core formation on the Hf-W isotopic composition of the Earth and dating of the Moon-forming impact. *Earth and Planetary Science Letters* **499**, 257–265 (2018).

82. Thiemens, M., Sprung, P., Fonseca, R., Leitzke, F. & Münker, C. . *Nature Geoscience* (2019).

83. Touboul, M., Puchtel, I. S. & Walker, R. J. Tungsten isotopic evidence for disproportional late accretion to the Earth and Moon. *Nature* **520**, 530–533 (2015).

84. Kruijer, T. S., Kleine, T., Fischer-Gödde, M. & Sprung, P. Lunar tungsten isotopic evidence for the late veneer. *Nature* **520**, 534–537 (2015).

85. Dauphas, N. & Marty, B. Inference on the nature and the mass of Earth's late veneer from noble metals and gases. *Journal of Geophysical Research (Planets)* **107**, 5129 (2002). astro-ph/0109309.

86. Dauphas, N. The isotopic nature of the Earth's accreting material through time. *Nature* **541**, 521–524 (2017).

87. Bergin, E. A., Blake, G. A., Ciesla, F., Hirschmann, M. M. & Li, J. Tracing the ingredients for a habitable earth from interstellar space through planet formation. *Proceedings of the National Academy of Science* **112**, 8965–8970 (2015). 1507.04756.

88. Chassefière, E. Loss of Water on the Young Venus: The Effect of a Strong Primitive Solar Wind. *Icarus* **126**, 229–232 (1997).